

Control of artificial pinning centers in REBCO coated conductors derived from the trifluoroacetate metal-organic deposition process

T Izumi^{ID} and K Nakaoka

National Institute of Advanced Industrial Science and Technology, 1-2-1 Namiki, Tsukuba, Ibaraki, Japan

E-mail: teruo.izumi@aist.go.jp

Received 17 August 2017, revised 23 October 2017

Accepted for publication 28 November 2017

Published 14 February 2018



Abstract

The metal-organic deposition (MOD) process using metal trifluoroacetate salts (TFA) has the advantages of low-cost and high-scalability for the fabrication of $\text{REBa}_2\text{Cu}_3\text{O}_y$ (REBCO, RE: rare earth elements) superconducting coated conductors (CCs) with high critical current density, in principle, because of its non-vacuum process. For the magnetic applications of CCs such as motors, magnetic resonance imaging and superconducting magnetic energy storage, further improvement of superconducting performance under magnetic fields is required. However, the in-field superconducting performance of REBCO CCs derived from the TFA-MOD process had been inferior to those derived from the vapor-phase process. In order to improve the in-field performance, the size control of the artificial pinning centers has been known as an effective way. In the early stage, the BaZrO_3 (BZO) material, which was one of the effective materials in the CCs by the vapor-phase process, was also introduced in the TFA-MOD-derived CCs. The unique feature of the BZO material in the TFA-MOD process is the shape. The BZO in the TFA-MOD process formed the particle shape, although in the vapor-phase process it has a rod shape with a long axis elongating along the thickness direction. In addition, a special heat treatment for refining the BZO particles was developed, which is called the ‘interim heat treatment’. This heating profile made the in-field characteristics higher, although they were still lower than those of the vapor-phase process. Then, the new MOD process including ‘ultra-thin once coating’ was recently developed for further refinement of the BZO particles. The characteristics of the new TFA-MOD-derived CCs in magnetic fields have become compatible with those of the CCs derived from the vapor-phase process.

Keywords: superconductor, tape, critical current, pinning center, MOD

(Some figures may appear in colour only in the online journal)

1. Introduction

Since the discovery of high T_c superconducting material by Bednorz and Muller in 1986 [1], the new materials with higher T_c had been found in sequence and some of them revealed the higher T_c over the liquid nitrogen temperature [2–7]. This made us expect large-scale applications in the wider field using the high T_c superconductors, although the real use of superconductivity has been limited in fields such as magnetic resonance imaging. $\text{REBa}_2\text{Cu}_3\text{O}_y$ (REBCO, RE: rare earth elements)

material is one of the materials with high T_c over 77 K. In addition, this material has the essentially superior feature of the critical current density (J_c) compared with others, especially for those in the magnetic field ($J_c(B)$) at relative high temperature. However, a well-textured oriented structure, which has biaxial orientation, is necessary to effectively use the advantage of this material. In order to satisfy the requirement in the wire/tape style, which is necessary for a lot of applications, the layered structure on the metal tape is selected and is called a coated conductor (CC). In this structure, several techniques have been

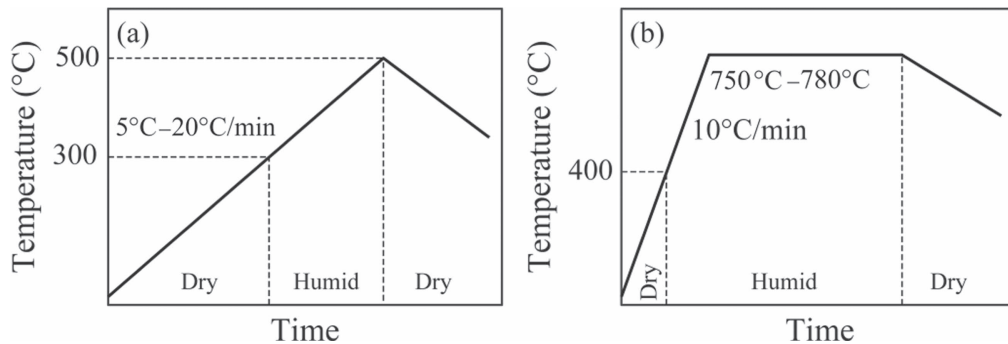


Figure 1. Typical heating profiles for the (a) calcination and (b) crystallization steps in the general TFA-MOD method.

developed to add the biaxial textured structure. The most popular one is the deposition of the well-textured buffer layer by ion-beam assisted deposition even on the non-textured substrate [8, 9]. The other one is the rolling-assisted biaxially textured substrate, in which the texturing is introduced in the metal substrate by a suitable cold rolling and heat treatment to the face-centered cubic metal tape [10]. On the other hand, several different deposition techniques have been developed for the REBCO superconducting layer, such as pulsed-laser deposition (PLD) [11–13], metal-organic chemical vapor deposition (MOCVD) [14, 15], metal-organic deposition (MOD) [16–18], and reactive co-evaporation deposition [19]. The development of CCs took place through competition in national projects in the United States and Japan in the first ten years from about 2000. Since then, new groups from other areas such as Korea [19] and the European Union [12, 20, 21] have participated in its development. In the early stages, the development took place with the aim of achieving a large number of the $I_c \times L$ products, where I_c is the critical current at 77 K under self-field and L is the length of the CCs. Through much effort to obtain long tape with a high I_c value, the $I_c \times L$ product has risen and reached over 600 kA m^{-1} ($I_c > 600 \text{ A cm}^{-1}$, $L > 1000 \text{ m}$) with several groups [22, 23]. Then, some companies began to sell CCs and the development of some applications using the CCs were also implemented such as in transmission cable, motors, generators, transformers, current limiters, and for superconducting magnetic energy storage. Because many of them use magnetic field, the specification of higher I_c properties under the magnetic field is an essential requirement. In order to improve the in-field performance, the introduction of artificial pinning centers (APCs) is known to be effective [24–27]. In this field, BaMO₃ (BMO, M: metal) is a well-known material, which is effective for improving the in-field performance. This approach has been employed in vapor-phase processing such as PLD and MOCVD, and has led to excellent results [26–29]. The specific feature of this kind of APC is the shape of the rod. Therefore, this type of APC is effective for improving the performance under external magnetic field (B) condition around the $B \parallel c$ -axis of the REBCO layer.

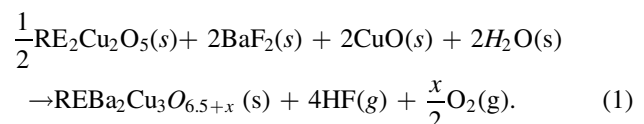
On the other hand, the application always needs to be low-cost. From this point of view, the MOD process is recognized as being cost-effective, because it does not need an expensive chamber and a special thermal source. Therefore, if the requirement of high in-field performance can be satisfied in the cost-effective MOD process, it should contribute to the progress

of the realization of applications using CCs. However, the CCs fabricated by the MOD process has revealed lower in-field performance than those produced by the vapor-phase processes.

In this paper, the recent progress by our group in the development of the MOD process for long CCs fabricated on buffered metal substrates to improve the in-field performance is reviewed.

2. Fundamentals of R&D on the TFA-MOD process

The MOD process using trifluoroacetate salts (TFA-MOD) as a starting solution has been developed for the epitaxial growth of REBCO superconducting films [16]. The TFA-MOD process is based on the chemical solution deposition process, which includes two stages: (1) coating of the starting solution on the textured metal substrate by appropriate techniques (such as spin coating, dip coating and slot-die coating); (2) heat treatment of the coated starting solution. Generally, the heat treatment of the TFA-MOD process involves calcination and crystallization steps. In the calcination step, the coated starting solution is thermally decomposed to an amorphous phase at relatively low temperature. The amorphous phase is crystallized to the REBCO phase via the crystallization step at high temperature. Figure 1 shows typical heating profiles for the calcination and crystallization steps in the general TFA-MOD process. The special feature of this system is the conversion reaction through BaF₂ for the formation of the superconducting phase as the following reaction:



Because, in the general MOD process, the reaction is basically controlled by the temperature, epitaxial growth is usually difficult in the thick film. However, the conversion system with consuming H₂O and discharging HF gas is necessary for the above system and it can make the epitaxial growth possible on the textured substrate. Therefore, a high J_c film can be obtained in the films fabricated by the TFA-MOD process.

The details of the reaction in this system were investigated in the early stage of R&D [30–32]. Figure 2 shows the

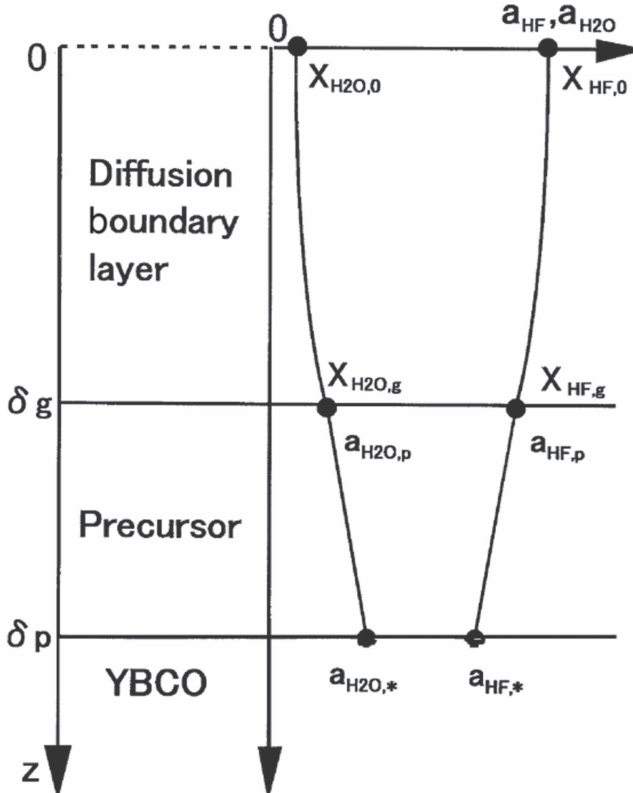


Figure 2. Schematic image of the theoretical analysis of YBCO growth during post-annealing in the TFA-MOD process considering both the diffusion in the gas boundary layer and the growth kinetics at the precursor/YBCO interface [30].

one-dimensional (1D) physical image of the mass transfer model for the growth of the REBCO film through the TFA-MOD process.

The REBCO film epitaxially grows from the interface of the precursor and the top of the buffer layer, and a boundary diffusion layer exists on the surface of the precursor. The H₂O is supplied from the gas outside of the boundary layer and diffuses into the growing interface of the REBCO layer through the diffusion boundary layer and the precursor film. The reaction of equation (1) takes place at the growing interface with consuming H₂O. The reaction spontaneously generates HF gas. It diffuses in the opposite route to H₂O and is removed by the outside gas flow. The growth rate can be indicated by the linking mass diffusion flows in the layers. In addition, the expression can be simplified by the important experimental result, which is independent of the growth rate on the film thickness, as follows [33]:

$$R \propto \frac{(V_g \cdot P_{H_2O})^{1/2}}{P_t} \quad (2)$$

where R is the growth rate in the vertical direction, V_g is the gas flow rate outside of the boundary layer, P_{H_2O} is the partial pressure of humidity and P_t is the total pressure. The prediction of the growth rate is important not only for prediction of the production rate but the control of the microstructure including REBCO crystallinity, APC, and pore, etc.

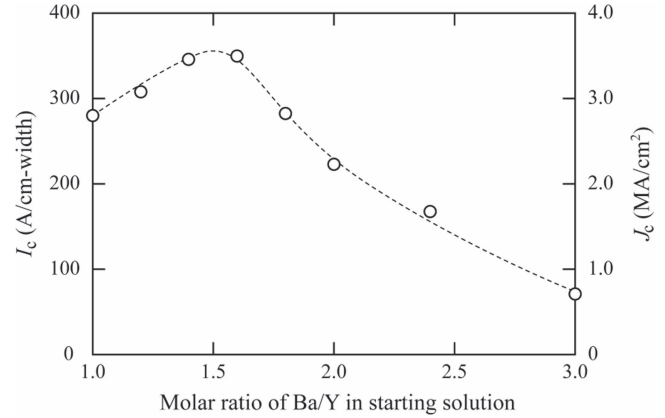


Figure 3. Relationship between molar ratios of Ba/Y in the starting solution and I_c and J_c values of the YBCO films with 1 μm in thickness at 77 K and self-field [35].

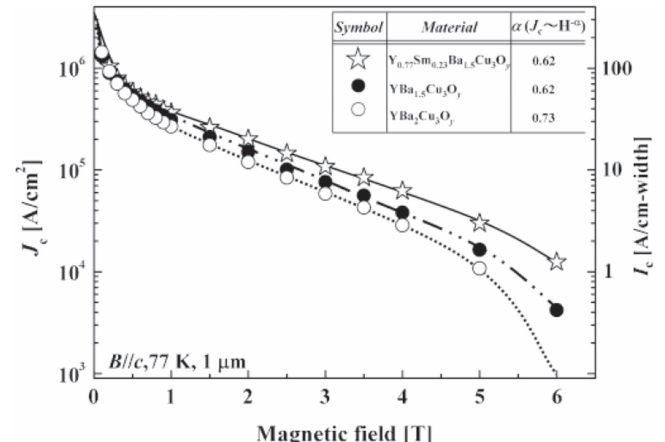


Figure 4. Magnetic field dependence of J_c and I_c measured for $B \parallel c$ at 77 K for 1 μm -thick YSmBCO CC, compared with YBCO CCs with stoichiometric and Ba-deficient composition [36].

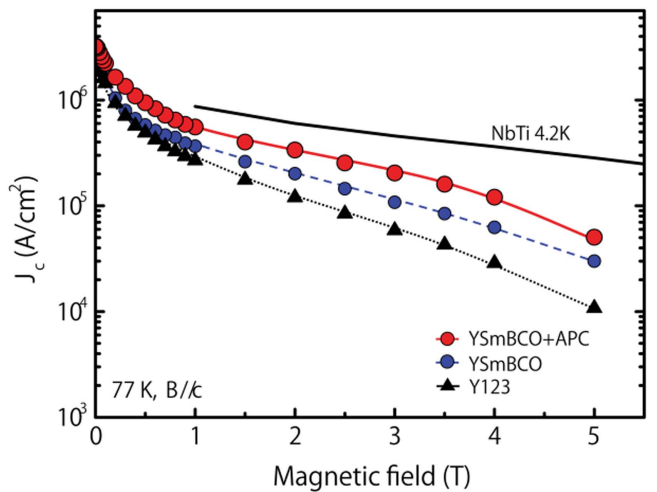


Figure 5. Magnetic field dependence of J_c values measured for $B \parallel c$ at 77 K in the YSmBCO + BZO CCs compared with those for the YBCO, YSmBCO CCs and a NbTi wire measured at 4.2 K [38].

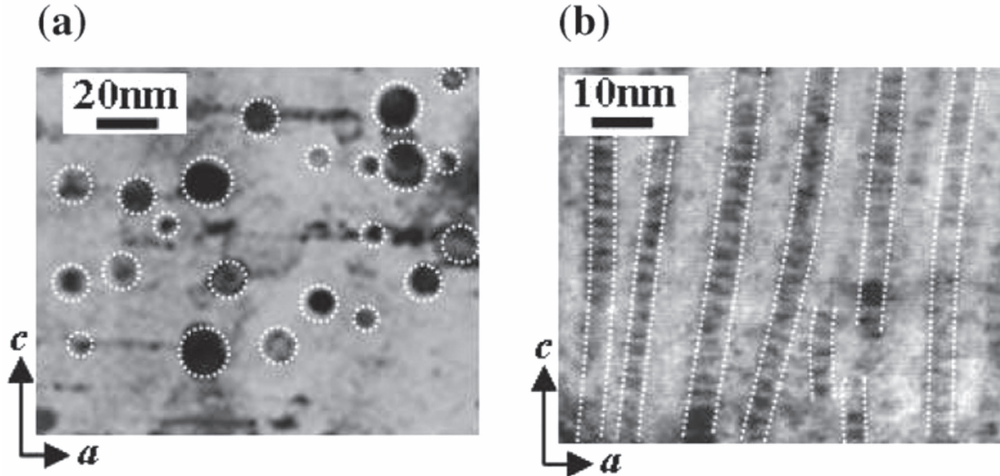


Figure 6. Cross-sectional TEM images of the (a) YSmBCO + BZO CCs fabricated by TFA-MOD. Some BZO particles are indicated by the white circles. And (b) of GdBCO + BZO CCs by PLD. The dark rods are the BZO phase, which are marked by the white dotted lines [40].

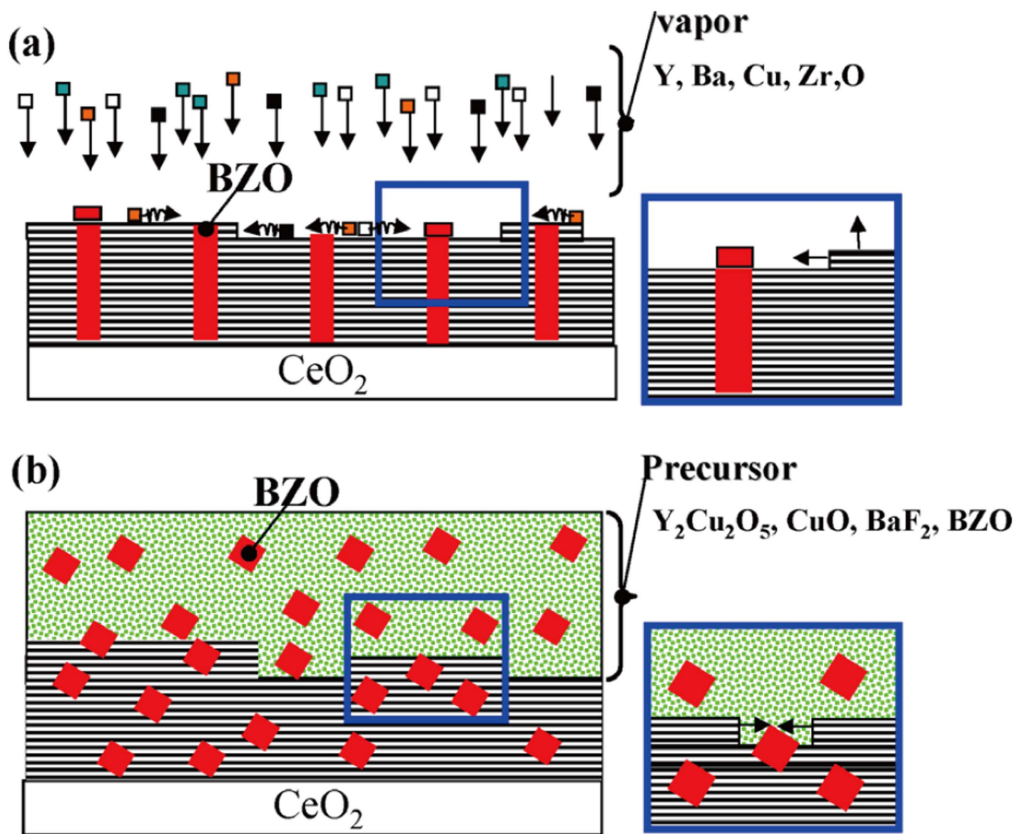


Figure 7. Schematic drawings of the formation mechanism of BZO in (a) the PLD process and (b) the TFA-MOD process, which were inferred from XRD patterns and TEM images [41].

In the next step, the J_c (self-field) and J_c (B) were improved by the compositional control in the TFA-MOD films [34–37]. Figure 3 shows the dependence of I_c and J_c values at 77 K and the self-field on the Ba-ratio to the Y in the starting solution. The Ba-ratio of 2.0 is the stoichiometric composition of the superconducting phase. However, the highest I_c value was recognized at the Ba-deficient composition from the stoichiometric one, as Ba-ratio is 1.5. Figure 4

shows the J_c dependence of the external magnetic field of the films with different Ba-ratios of 2.0 and 1.5. This can be predicted by microstructure analysis. If some Ba elements, which might be segregated at the grain boundary, are unreacted and remained in the films, the J_c property should be lower. Therefore, the Ba-deficient composition can suppress the remaining Ba element and improve the connectivity of the grains.

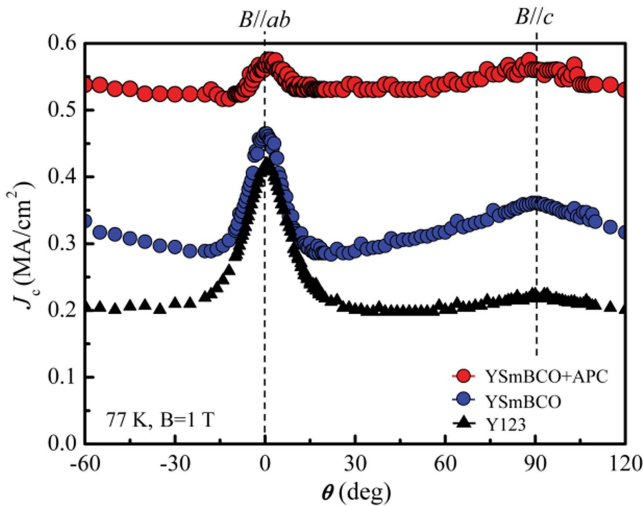


Figure 8. Field angular dependence of $J_c(B)$ at 77 K and $B = 1$ T for the YSmBCO + APC CCs compared with that for the YBCO and YSmBCO CCs. As indicated in the figure, $\theta = 0^\circ$ corresponds to $B \parallel ab$ and $\theta = 90^\circ$ corresponds to $B \parallel c$ [38].

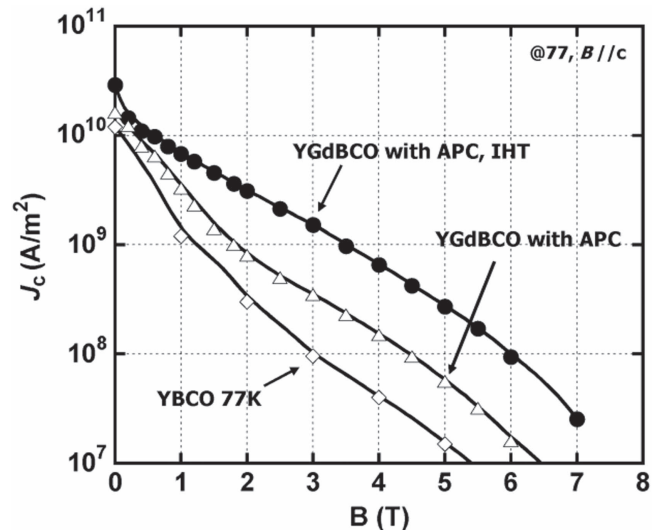


Figure 10. $J_c(B \parallel c)$ properties of YGdBCO + BZO CCs with IHT compared with YGdBCO + APC and YBCO prepared by the conventional heating profile [44].

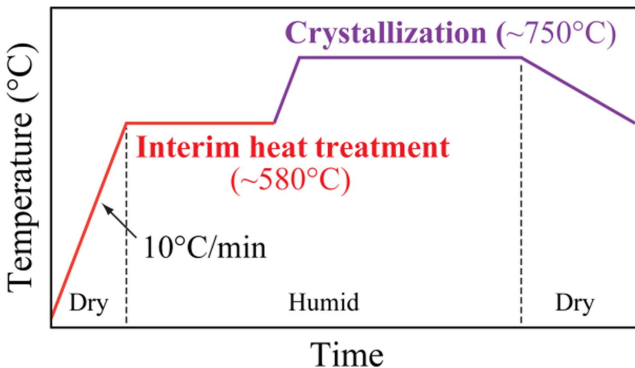


Figure 9. Typical heating profiles for the crystallization process with the IHT step.

3. Early stage of R&D for the introduction of APC in TFA-MOD

As described in the Introduction, the effectiveness of the APC of BMO materials (BMO-APC) had already been confirmed by vapor-phase processing in the early 2000s. Concerning MOD films, there was an attempt to introduce BMO-APC around 2008. It was clarified that BMO is also effective for the improvement of in-field performance even in the APC of MOD films, as shown in figure 5 [38–40]. Ba-deficient (Ba-ratio of 1.5) starting solution was also used for R&D for the introduction of APC in TFA-MOD. However, in order to correct the consumption of the Ba element due to the BMO formation, Ba concentration in the starting solution was increased by the same molar amount as the added ‘M’.

The shape of BMO-APC in the MOD films is clearly different from that in the films by vapor-phase processing such as the PLD. Figure 6(a) shows the cross-sectional microstructure of the MOD films with BZO-APC (Zr: Zr). The

BZO has particle shape, although the same BZO in the PLD films shows rod shapes, as shown in figure 6(b).

Figure 7 shows the schematic ideas for explaining the reason for the difference of BMO shape based on the growth mechanism. In the PLD system, both phases of REBCO and BMO are the same growing interface. The growth components of REBCO and BMO should seek a suitable position as a crystal on the growing interface for minimizing the interfacial energies. Therefore, each phase should select the position on the crystal interface of the same phase under the conditions of reasonable low supersaturation of the growth. As a result, BMO crystal naturally continued and formed a rod shape and the relationship on the crystal orientation between REBCO and BMO is maintained in the films. On the other hand, the BMO particles randomly nucleate in the precursor films prior to the growth of the REBCO films in the TFA-MOD process [41]. Then, the REBCO films grow epitaxially on the CeO₂ surface with entrapping the preliminarily grown BMO particles. As a result, the BMO phase has the particle shape without any relationship of the crystallographic orientation in the TFA-MOD films.

As reflected in the shape of BZO, the magnetic-field angular dependence of J_c is more isotropic compared with that of the films by the PLD method, as shown in figure 8.

4. Interim heat treatment

As mentioned in the above section, the $J_c(B)$ performance was also improved by the introduction of APC into MOD films. However, the achieved $J_c(B)$ value is lower than that in the PLD films. For the purpose of further improvement of the $J_c(B)$ performance in MOD-derived CCs, the refinement and homogeneous distribution of APCs by modifying the heating process has been investigated in several research groups [42–45]. We found the effective heat-treatment step, interim

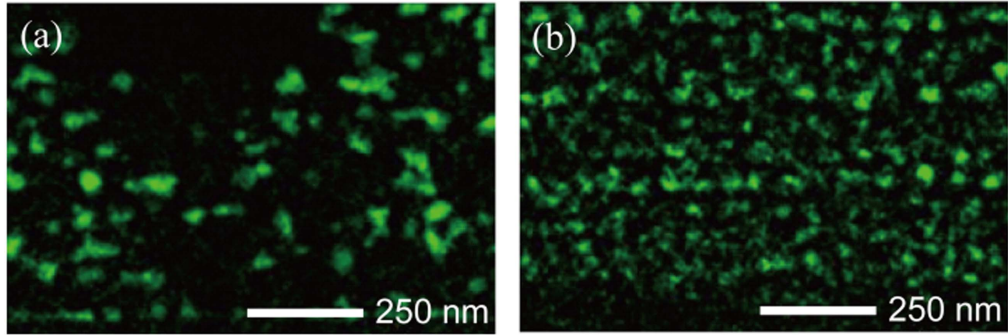


Figure 11. EDS mappings of the Zr element in YGdBCO + BZO CCs fabricated (a) without and (b) with the IHT process [45].

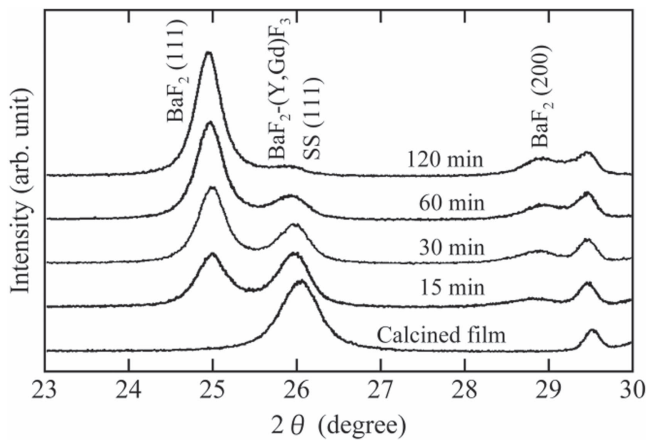


Figure 12. XRD patterns of the calcined film and the quenched samples during the IHT process [45].

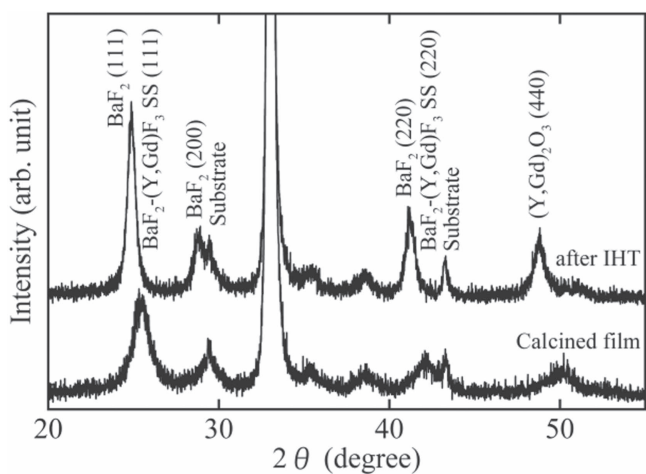


Figure 13. XRD patterns of the calcined film and the film after the IHT process [45].

heat treatment (IHT), for the fabrication of the YGdBCO + BZO system in the TFA-MOD method [44, 45]. The IHT was applied once in the water vapor gas flow to the calcined films prepared by the multi-coating/calcination process before the YGdBCO phase crystallization step at the temperature of $\sim 580^\circ\text{C}$, which is higher than the maximum

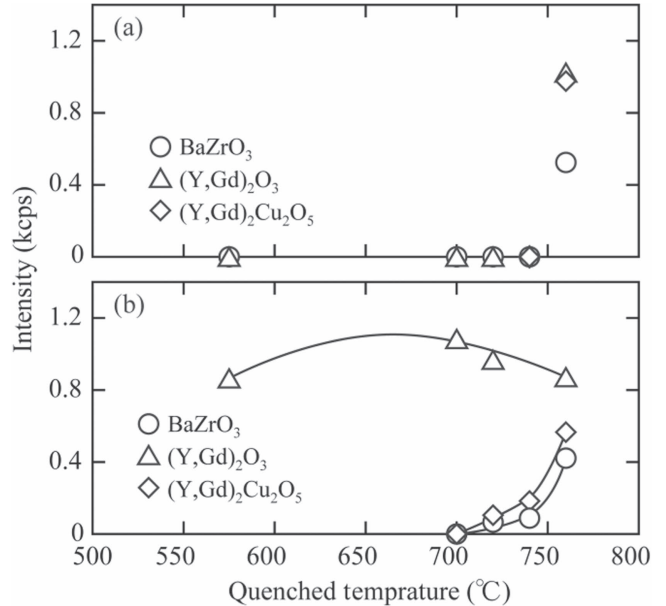


Figure 14. Relationship between the XRD peak intensities of the BZO, $(\text{Y},\text{Gd})_2\text{O}_3$, and $(\text{Y},\text{Gd})_2\text{Cu}_2\text{O}_5$ phases in the quenched samples and quenched temperature during the crystallization process (a) without and (b) with IHT [45].

temperature of the calcination step ($\sim 500^\circ\text{C}$) and lower than the crystallization temperature of the YGdBCO phase ($\sim 750^\circ\text{C}$). The heating profiles for the crystallization step including the IHT step are schematically shown in figure 9.

Figure 10 shows the J_{c} ($B \parallel c$) performance at 77 K of YBCO and YGdBCO + BZO CCs fabricated with and without IHT. The J_{c} ($B \parallel c$) characteristic of the CCs was evidently improved by the introduction of IHT at all applied magnetic fields. Figure 11 shows energy dispersive spectroscopy (EDS) mappings of the Zr element of CCs (a) without and (b) with IHT, and these Zr-related particles are recognized as the BZO phase due to the selected-area diffraction pattern analysis of those particles [41]. These EDS mappings show that the IHT process is effective for the uniform dispersion of finer BZO particles in the YGdBCO matrix.

As a next step, the reactions and role of IHT has been investigated. Figure 12 shows XRD patterns of the calcined film and the quenched samples, which were prepared by

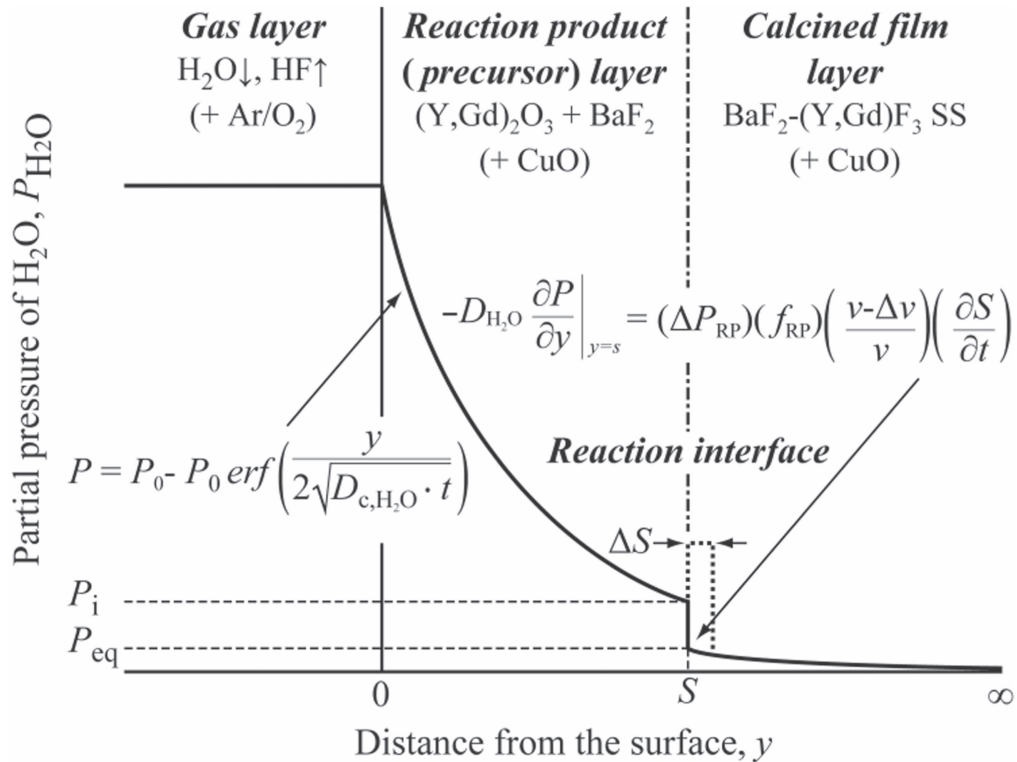


Figure 15. Schematic outline of the numerical analysis for the kinetics in the IHT process (P_0 is the H_2O partial pressure at the surface, S is the distance from the surface to the reaction interface, t is the time at the IHT step period, $(v-\Delta v)/v$ is the volume shrinkage ratio after the reaction, ΔP_{RP} is the required H_2O gas mole fraction (partial pressure) for the differential unit volume of the reaction product, f_{RP} is the volume fraction of the reaction product in the precursor layer, and $D_{\text{H}_2\text{O}}$ is the H_2O gas Knudsen diffusion co-efficient in the capillary pores in the reaction product layer) [45].

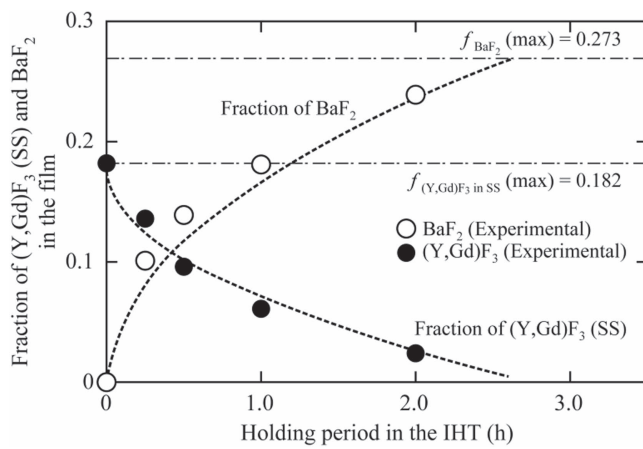


Figure 16. Relationship between the fraction of $(\text{Y},\text{Gd})\text{F}_3$ (in SS of $\text{BaF}_2-(\text{Y},\text{Gd})\text{F}_3$) and BaF_2 in the film and holding time in the IHT step [45].

cooling them rapidly after holding them for 15–120 min at 575 °C during the IHT process. The (111) peak of the $\text{BaF}_2-(\text{Y},\text{Gd})\text{F}_3$ solid solution (SS) phase ($2\theta \sim 26^\circ$) was observed in the calcined film. As for the quenched samples, pure BaF_2 phase was detected and the peak intensities of the pure BaF_2 phase increased, while those of the $\text{BaF}_2-(\text{Y},\text{Gd})\text{F}_3$ SS phase decreased as the holding time during the IHT process increased. XRD patterns scanned over the relatively broad range of 23°–55° for the calcined film and the film after

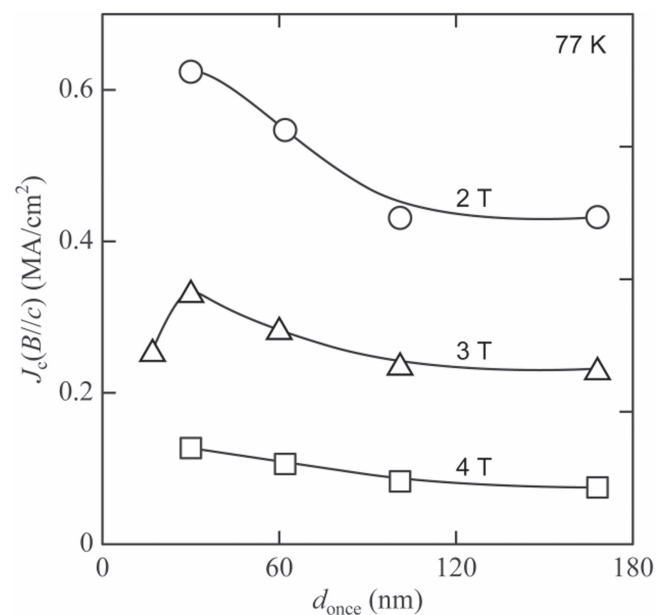


Figure 17. d_{once} dependence of $J_c(B \parallel c)$ values of the YGdBCO + BZO films at 77 K, where the applied magnetic fields were 2, 3, and 4 T [46].

the IHT step are shown in figure 13. When the calcined films were applied to the IHT process, it was noted that the $\text{BaF}_2-(\text{Y},\text{Gd})\text{F}_3$ SS decomposed to generate the $(\text{Y},\text{Gd})\text{O}_3$ phase with the pure BaF_2 phase as a result of the

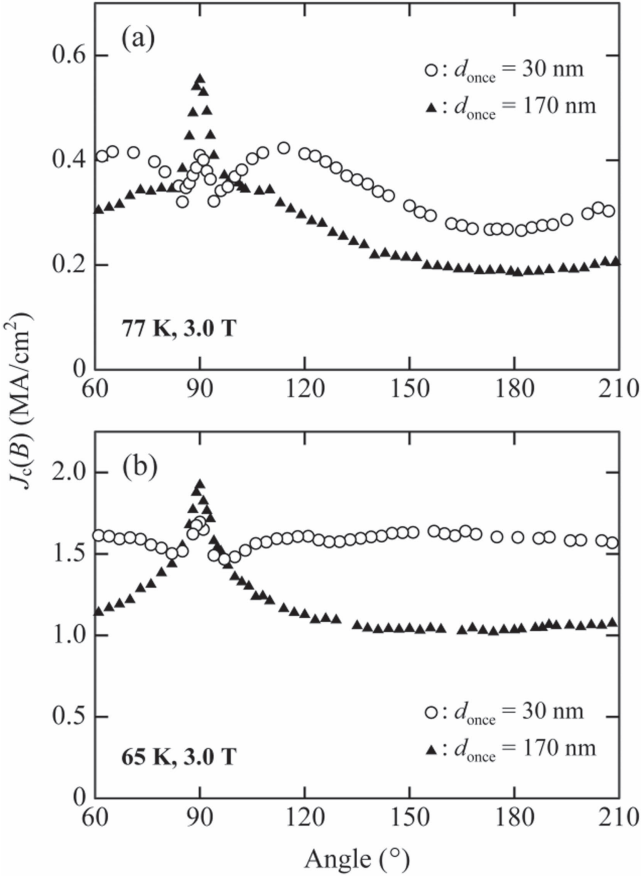
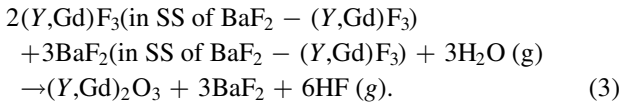


Figure 18. Magnetic-field angular dependence of $J_c(B)$ at (a) 77 and (b) 65 K and 3 T for the YGdBCO + BZO CCs fabricated by the different d_{once} conditions of 30 and 170 nm [47].

disappearance of the $(Y,\text{Gd})\text{F}_3$ phase from the $\text{BaF}_2-(Y,\text{Gd})\text{F}_3$ SS. Therefore, the basic reaction in the IHT process was found to be as follows:



XRD peak intensities of the BZO, $(Y,\text{Gd})_2\text{O}_3$, and $(Y,\text{Gd})_2\text{Cu}_2\text{O}_5$ phases in the quenched samples, which were prepared by cooling rapidly at 575 °C–760 °C during the crystallization step (a) without and (b) with IHT are shown in figure 14. The BZO, $(Y,\text{Gd})_2\text{O}_3$, and $(Y,\text{Gd})_2\text{Cu}_2\text{O}_5$ phases were not observed by 760 °C in the quenched sample without IHT. On the other hand, the $(Y,\text{Gd})_2\text{O}_3$ phase was recognized in the entire temperature range. And the BZO and $(Y,\text{Gd})_2\text{Cu}_2\text{O}_5$ phases were formed at lower temperature than the YGdBCO phase crystallization temperature (~750 °C) in the films with IHT. The crystallization reaction to generate the BZO and YGdBCO phase crystals after the IHT process can be expressed by the following equations:

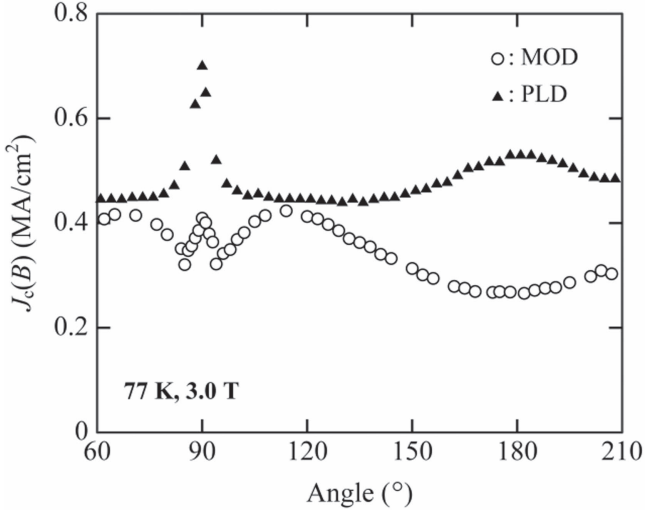
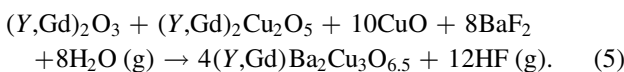


Figure 19. Magnetic-field angular dependences of $J_c(B)$ at 77 K and 3 T for the MOD – YGdBCO + BZO CCs fabricated with d_{once} conditions of 30 nm and PLD – EuBCO + BHO.

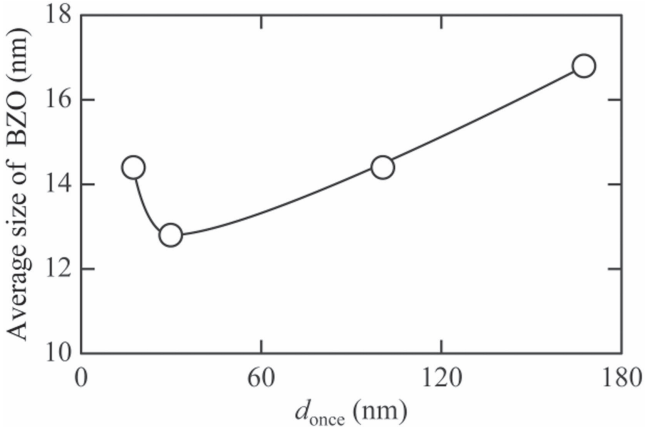


Figure 20. d_{once} dependence of the average size of the BZO particles in the YGdBCO + BZO CCs analyzed from TEM observations [46].

In the case without IHT, the crystallization reactions of the BZO and YGdBCO phases indicated in equations (4) and (5) are considered to be basically almost the same temperature as the results of the quench experiments. Accordingly, equation (3) occurs during the heating period or early in the holding period of the crystallization process, and which leads to coarsening of the BZO particles owing to equation (4) occurring at high temperature.

As the effects of the IHT process, the temperature of the nucleation and the growth of the BZO particles is lowered due to the completion of the transformation from $(Y,\text{Gd})\text{F}_3$ to $(Y,\text{Gd})_2\text{O}_3$ by the addition of the IHT step. The low temperature means a large supersaturation but low diffusivity, which leads to fine particle size of BZO. If the $(Y,\text{Gd})\text{F}_3$ phase exists in the precursor as a heating pattern without the IHT step, the H_2O gas should be primarily used for the transformation rather than the reaction for the nucleation of the BZO phase.

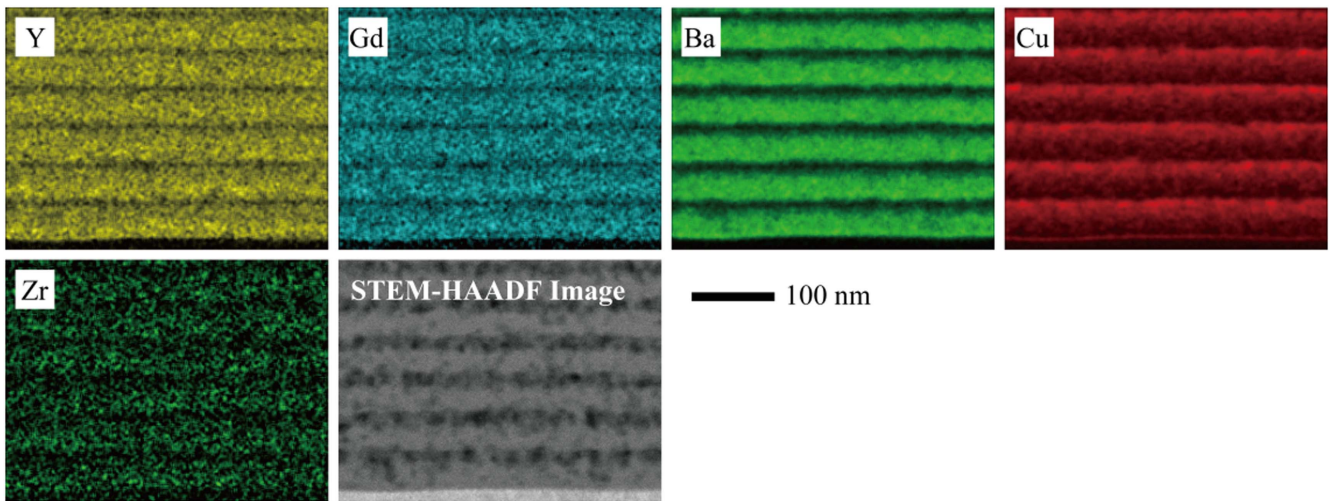


Figure 21. EDS elemental maps of the calcined films with d_{once} condition of 30 nm [47].

Table 1. Experimental results for the average size of the BZO particles and J_c properties of samples fabricated with different final thickness of one coating.

d_{once}	BZO average size (nm)	J_c @ 77 K, s. f. (MA cm^{-2})	J_c ($B \parallel c$) @ 77 K, 3 T (MA cm^{-2})	J_c ($B \parallel c$) @ 65 K, 3 T (MA cm^{-2})
17	14.4	4.74	0.26	—
30	12.8	4.60	0.27	1.60
60	—	4.53	0.23	—
100	14.4	4.26	0.19	1.04
140	—	4.45	0.19	—
170	16.8	4.48	0.19	1.04

The 1D theoretical analysis of the reaction kinetics in the IHT process considering the diffusion of H_2O gas and growth kinetics at the interface between the reaction product (precursor) layer and the calcined film layer was carried out. Figure 15 shows the physical image for the quantitative analysis of the IHT process. It was presumed that the reaction of equation (3) only occurs at the interface between the precursor layer and the calcined layer, and that the produced HF diffuses back out through the formed precursor layer. Under the conditions of $P_{\text{H}_2\text{O}} = 0.042 \text{ atm}$ and IHT temperature of 575°C , the following equation was estimated by theoretical analysis [45]:

$$S = 1.81 \times 10^{-11} \cdot t^{1/2} \quad (6)$$

where S and t represent the distance from the surface to the reaction interface and time at the IHT step period, respectively. In order to verify the theoretical predictions estimated by equation (6), the experimental results, which are estimated from the XRD patterns of figure 12, are compared with the simulation. The calculated volume fractions of $(\text{Y},\text{Gd})\text{F}_3$ (in SS of $\text{BaF}_2-(\text{Y},\text{Gd})\text{F}_3$) and BaF_2 are plotted in broken lines in figure 16. The calculated results agree very well with the experimental results.

5. Ultra-thin once-coating MOD (UTOC-MOD) process

As mentioned above, it was found that the IHT process is effective for improving in-field J_c performance. However, it was still lower than that in the CCs fabricated by PLD. Then, we found a hint of further improvement of J_c (B) performance in TFA-MOD films. In the EDS mapping image of the Zr element of the CC with IHT, as shown in figure 11, BZO particles formed the dotted lines parallel to the CeO_2 interface, which correspond to the numbers of the multi-coating/calcnination process. This means that the line distribution might be caused by the repetition of the multi-coating/calcnination process. This suggested the possibility of obtaining smaller BZO particles by the thinning of the once-coated film thickness (d_{once}) in the multi-coating/calcnination process. Then, the influence of d_{once} on BZO particle size was investigated. Here, the thickness of d_{once} is the film thickness for once coating, which is converted into a film thickness after the crystallization.

The films were fabricated with different d_{once} conditions from 170–17 nm, where d_{once} of 170 nm was the standard condition in the previous study. The number of repetition times of a series of spin-coating/calcnination to get the same total film thickness of $\sim 0.6\text{--}0.7 \mu\text{m}$ are four (for $d_{\text{once}} = 170 \text{ nm}$), five (for $d_{\text{once}} = 140 \text{ nm}$), six (for $d_{\text{once}} = 100 \text{ nm}$), 20 (for $d_{\text{once}} = 30 \text{ nm}$) and 35 (for $d_{\text{once}} = 17 \text{ nm}$).

Figure 17 shows the d_{once} dependence of J_c ($B \parallel c$) at 77 K and 3 T for YGdBCO + BZO CCs fabricated by different d_{once} conditions with IHT. The J_c ($B \parallel c$) values increased as d_{once} decreased to 30 nm. The CC fabricated with $d_{\text{once}} = 30 \text{ nm}$ had a high J_c ($B \parallel c$) of 0.27 MA cm^{-2} at 77 K and 3 T, which is 1.6 times higher than that under the standard condition of $d_{\text{once}} = 170 \text{ nm}$. However, the tendency was not maintained for the sample with $d_{\text{once}} = 17 \text{ nm}$. It exhibited almost the same or slightly lower J_c ($B \parallel c$) value than that with $d_{\text{once}} = 30 \text{ nm}$. In the magnetic-field angular dependence of the J_c (B) property, the high value of the minimum J_c (B)

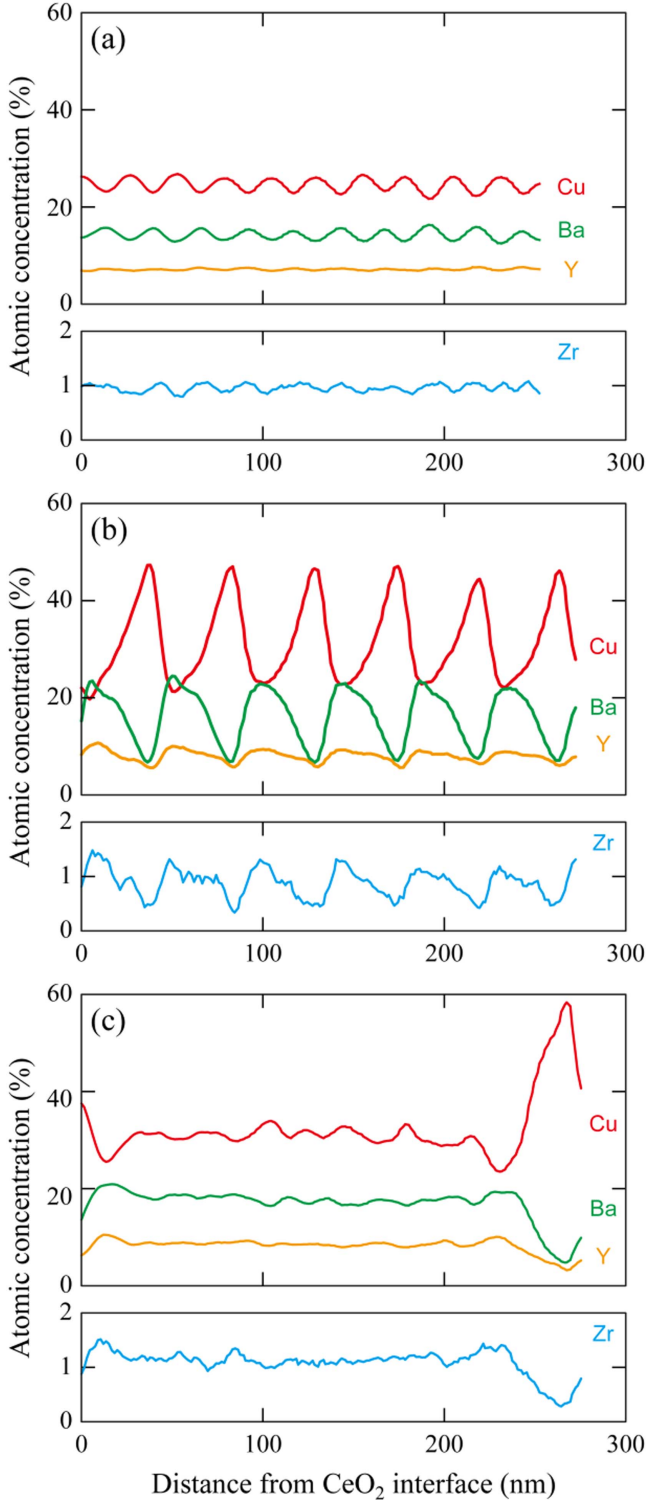


Figure 22. Elemental concentration line profiles along the depth direction of the precursors fabricated with different d_{once} conditions of (a) 17, (b) 30, and (c) 170 nm, which were analyzed from TEM observation [46].

was also obtained for the CC fabricated with $d_{\text{once}} = 30$ nm, and the magnetic-field angular dependence is quasi-isotropic within almost all the angles (figure 18). Figure 19 shows the magnetic-field angular dependence of $J_c(B)$ at 77 K, 3 T for MOD-derived YGdBCO + BaZrO₃ with $d_{\text{once}} = 30$ nm and

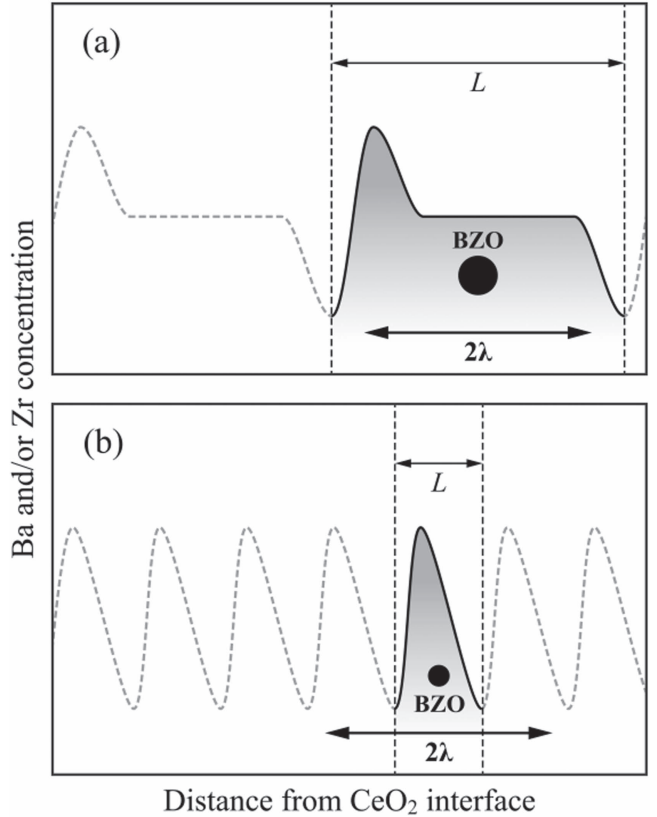


Figure 23. Schematic illustrations of the refining mechanism of BZO particles by the thinning of d_{once} [47].

PLD-derived EuBCO + BaHfO₃ CCs fabricated in our laboratory. The PLD-derived CC exhibited the broad peak of $J_c(B)$ around $B \parallel c$ compared with the MOD-derived CC, which might be due to the rod-like shape of BHO-APC. The $J_c(B \parallel c)$ and minimum $J_c(B)$ values of PLD – EuBCO + BHO at 77 K, 3 T were 0.53 and 0.44 MA cm⁻², respectively. In addition, the $J_c(B \parallel c)$ value at 77 K, 3 T for MOCVD – YGdBCO + BZO CC was 0.7 MA cm⁻² [48]. According to the development of the new process (UTOC-MOD process), the $J_c(B)$ values were still inferior to the MOCVD, but improved to a competitive level when compared to the PLD.

The d_{once} dependence of the average size of the BZO particles calculated from cross-sectional TEM observations of CCs is shown in figure 20. Although the average BZO particle size decreased as d_{once} decreased to 30 nm, the size of the sample with $d_{\text{once}} = 17$ nm was slightly larger than that with $d_{\text{once}} = 30$ nm. The refining size of the BZO particles means their increase of density, which could make the $J_c(B)$ property improve, and the trend in the average BZO particle may correspond to that of the $J_c(B \parallel c)$ property in figure 17. The $J_c(B)$ characteristics and the size of the BZO particles are summarized in Table 1. According to the development of the new process (UTOC-MOD process), the $J_c(B)$ values were improved to a competitive level when compared to the PLD films.

EDS elemental maps of the main constituent elements (Y, Gd, Ba, Cu, and Zr) in the precursor films with

$d_{\text{once}} = 30 \text{ nm}$ are shown in figure 21 as the fundamental information for considering the refining mechanism. Although the mechanism and/or its kinetics have not been understood yet, EDS elemental maps could clearly identify the compositional segregation within the thickness of the once layer. Due to the investigation of the segregation in detail, EDS line-scan analysis along the thickness direction of Y, Ba, Cu, and Zr was performed on the calcined films with different d_{once} conditions of 170, 30, and 17 nm (figure 22). In the profiles of the calcined film with $d_{\text{once}} = 170 \text{ nm}$ (conventional condition), the Cu elemental peaks and the valleys of other elements are located at the same position and at an interval of d_{once} . The actual interval is larger than d_{once} (170 nm) since this is the calcined film before shrinkage, which occurred during the crystallization process. In addition, concentration plateaus between the peaks and valleys were observed. For the sample with $d_{\text{once}} = 30 \text{ nm}$, Cu peaks and other valleys were clearly observed and the interval becomes proportionally shorter than that for the calcined film with $d_{\text{once}} = 170 \text{ nm}$. In this sample, the plateau becomes narrow, and the peak height and valley depth are smaller than those of the calcined film with $d_{\text{once}} = 170 \text{ nm}$. Comparing the above-mentioned calcined films, the peaks and valleys were extremely suppressed, and a wave structure was barely observed for the calcined film with $d_{\text{once}} = 17 \text{ nm}$. Basically, the mechanism of refining of the BZO particles owing to thinning of d_{once} could be explained by the limited diffusion of the necessary elements due to the existence of the concentration valleys/peaks. Here, it is assumed that elements cannot diffuse over the valleys/peaks. If the interval between the valleys (L) is wider than twice the characteristic length for diffusion (λ), as schematically shown in figure 23(a), the nucleated BZO particles should grow freely. Many BZO particles can grow with the consumption of the elements in a region of 2λ . However, when the interval is narrower than 2λ , as schematically shown in figure 23(b), the quantities of necessary elements for growth are limited in the area within this interval. In this case, the growth should be suppressed, compared with the free growth mentioned above.

As a result, the BZO particles become finer compared with samples with a wide interval. This idea can explain the tendencies of the BZO particle size and related J_c (B) properties for a range of values of d_{once} from 170–30 nm. However, it is difficult to explain the behavior of the sample with $d_{\text{once}} = 17 \text{ nm}$. The wave structure can be barely recognized, but clear peaks and valleys could not be observed in the distribution of the elements of the sample with $d_{\text{once}} = 17 \text{ nm}$. In this sample, it appears that clear peaks and valleys due to segregation cannot be sufficiently formed because the interval is too short. Thus, the effect of the diffusion barrier due to the valleys/peaks becomes weaker than that in the other samples. Therefore, the BZO particle size in the sample with $d_{\text{once}} = 17 \text{ nm}$ is larger, and J_c (B) is almost the same as or slightly lower than that with $d_{\text{once}} = 30 \text{ nm}$. The refining mechanism mentioned above suggests that the finer BZO particles could be expected if the elemental valley/peak is formed even in the thinner d_{once} rather than the d_{once} of 30 nm.

6. Conclusion

We reviewed the recent progress in the improvement of the J_c performance of the TFA-MOD-derived REBCO CCs under magnetic field by the nanostructure control of APC materials. The in-field performance of REBCO CCs derived from the TFA-MOD process had been inferior to those derived from the vapor-phase process, which was a serious problem for magnetic applications of TFA-MOD-derived CCs. In the early stage of the R&D, we could confirm that the introduction of BMO-APC into the TFA-MOD film is effective for obtaining high J_c (B) properties. In addition, we made significant progress on the in-field J_c characteristics of the CCs, due to the development of the IHT and UTOC-MOD process. The IHT and UTOC-MOD processes provide homogeneous dispersion with refining of the BZO-APC materials, respectively, which leads to enhancement of the in-field J_c characteristics. As a result, the in-field performance of the TFA-MOD films reached a high level, which is comparable to the films made by the vapor-phase process. This indicates the possibility of fabricating low-cost and high-performance CCs, which is considered to lead to the development of the practical application of superconducting devices. However, in order to satisfy the required specifications of superconducting devices, it is still necessary to improve the in-field J_c performance, and further development can be expected.

Acknowledgments

This study was supported by the Ministry of Economy, Trade and Industry (METI), the Japan Agency for Medical Research and Development (AMED), and the New Energy and Industrial Technology Development Organization (NEDO).

ORCID iDs

T Izumi  <https://orcid.org/0000-0002-5470-1190>

References

- [1] Bednorz J G and Muller K A 1986 *Z. Phys. B* **64** 189–93
- [2] Takagi H, Uchida S, Kitazawa K and Tanaka S 1987 *Jpn. J. Appl. Phys.* **26** L123–4
- [3] Wu M K, Ashburn J R, Torng C J, Hor P H, Meng R L, Gao L, Huang C J, Wang Y Q and Chu C W 1987 *Phys. Rev. Lett.* **58** 908–10
- [4] Maeda H, Tanaka Y, Fukutomi M and Asano T 1988 *Jpn. J. Appl. Phys.* **27** L209–10
- [5] Sheng Z Z and Hermann A M 1988 *Nature* **332** 138–9
- [6] Schilling A, Cantoni M, Guo J D and Ott H R 1993 *Nature* **363** 56–8
- [7] Nagamatsu J, Nakagawa N, Maranaka T, Zenitani Y and Akimitsu J 2001 *Nature* **410** 63–4
- [8] Rossnagel S M and Cuomo J J 1987 *MRS Bull.* **12** 40–51
- [9] Iijima Y, Tanabe N, Ikeda Y and Kohno O 1991 *Physica C* **185–189** 1959–60
- [10] Goyal A *et al* 1996 *Appl. Phys. Lett.* **69** 1795–7

- [11] Wu X D *et al* 1995 *Appl. Phys. Lett.* **67** 2397–9
- [12] Usoskin A, Freyhardt H C, Issaev A, Dzick J, Knoke J, Oomen M P, Leghissa M and Neumueller H W 2003 *IEEE Trans. Appl. Supercond.* **13** 2452–7
- [13] Ibi A, Fukushima H, Yamada Y, Miyata S, Kuriki R, Takahashi K and Shiohara Y 2006 *Supercond. Sci. Technol.* **19** 1229–32
- [14] Selvamanickam V *et al* 2009 *IEEE Trans. Appl. Supercond.* **19** 3225–30
- [15] Holesinger T G, Maiorov B, Ugrulu O, Civale L, Chen Y, Xiong X and Selvamanickam V 2009 *Supercond. Sci. Technol.* **22** 045025
- [16] McIntyre P C, Cima M J, Smith R B, Hallock B, Siegel M P and Phillips J M 1992 *J. Appl. Phys.* **71** 1868–77
- [17] Izumi T *et al* 2007 *Physica C* **463–465** 510–4
- [18] Rupich M W *et al* 2010 *Supercond. Sci. Technol.* **23** 014015
- [19] Lee J H, Lee H, Lee J W, Choi S M, Yoo S I and Moon S H 2014 *Supercond. Sci. Technol.* **27** 044018
- [20] Dürrschnabel M, Aabdin Z, Bauer M, Semerad R, Prusseit W and Eibl O 2012 *Supercond. Sci. Technol.* **25** 105007
- [21] Obradors X and Puig T 2014 *Supercond. Sci. Technol.* **27** 044003
- [22] Igarashi M *et al* 2012 *Physics Procedia* **36** 1412–6
- [23] Oh S S, Kim H S, Ha H S, Ko R K, Ha D W, Lee H, Moon S H and Yoo S I 2013 *Progress in Superconductivity and Cryogenics* **15** 1–5
- [24] Matsushita T 2000 *Supercond. Sci. Technol.* **13** 730–7
- [25] Haugan T, Barnes P N, Wheeler R, Meisenkothen F and Sumption M 2004 *Nature* **430** 867–70
- [26] Macmanus-Driscoll J L, Foltyn S R, Jia Q X, Wang H, Serquis A, Civale L, Maiorov B, Hawley M E, Maley M P and Peterson D E 2004 *Nat. Mater.* **3** 439–43
- [27] Selvamanickam V, Xu A, Liu Y, Khatri N D, Lei C, Chen Y, Galstyan E and Majkic G 2014 *Supercond. Sci. Technol.* **27** 055010
- [28] Goyal A *et al* 2005 *Supercond. Sci. Technol.* **18** 1533–8
- [29] Tobita H, Notoh K, Higashikawa K, Inoue M, Kiss T, Kato T, Hirayama T, Yoshizumi M, izumi T and Shiohara Y 2012 *Supercond. Sci. Technol.* **25** 062002
- [30] Honjo T *et al* 2003 *Physica C* **392–396** 873–81
- [31] Honjo T, Nakamura Y, Teranishi R, Fuji H, Shibata J, Izumi T and Shiohara Y 2003 *IEEE Trans. Appl. Supercond.* **13** 2516–9
- [32] Nomoto S, Teranishi R, Honjo T, Izumi T and Shiohara Y 2005 *Mater. Trans.* **46** 922–9
- [33] Miura M, Ichikawa H, Sutoh Y, Nakaoka K, Yoshizumi M, Yamada Y, Izumi T and Shiohara Y 2009 *Physica C* **469** 1336–40
- [34] Izumi T *et al* 2007 *Physica C* **463–465** 510–4
- [35] Nakaoka K, Matsuda J, Kito Y, Goto T, Yanada Y, Izumi T and Shiohara Y 2007 *Physica C* **463–465** 519–22
- [36] Miura M *et al* 2008 *Physica C* **468** 1643–6
- [37] Izumi T, Yoshizumi M, Miura M, Nakaoka K, Ichikawa Y, Sutoh Y and Miyata S 2009 *Physica C* **469** 1322–5
- [38] Miura M, Kato T, Yoshizumi M, Yamada Y, Izumi T, Shiohara Y and Hirayama T 2008 *Appl. Phys. Express* **1** 051701
- [39] Miura M, Kato T, Yoshizumi M, Yamada Y, Izumi T, Shiohara Y and Hirayama T 2009 *Appl. Phys. Express* **2** 023002
- [40] Miura M, Kato T, Yoshizumi M, Yamada Y, Izumi T, Hirayama T and Shiohara Y 2009 *IEEE Trans. Appl. Supercond.* **19** 3275–8
- [41] Miura M, Yoshizumi M, Izumi T and Shiohara Y 2010 *Supercond. Sci. Technol.* **23** 014013
- [42] Coll M *et al* 2014 *Supercond. Sci. Technol.* **27** 044008
- [43] Horita H, Teranishi R, Yamafa K, Kaneko K, Sato Y, Otaguro, Nishiyama T, Izumi T and Awaji S 2017 *Supercond. Sci. Technol.* **30** 025022
- [44] Kimura K *et al* 2015 *IEEE Trans. Appl. Supercond.* **25** 6604204
- [45] Nakaoka K, Kimura K, Kato T, Yoshida R, Usui Y, Nakamura M, Izumi T and Siohara Y 2016 *IEEE Trans. Appl. Supercond.* **26** 800304
- [46] Izumi T, Nakaoka K, Yoshida R, Kimura K, Kato T, Miura M and Shiohara Y 2017 *IEEE Trans. Appl. Supercond.* **27** 6601604
- [47] Nakaoka K, Yoshida R, Kimura K, Kato T, Usui Y, Izumi T and Shiohara Y 2017 *Supercond. Sci. Technol.* **30** 055008
- [48] Selvamanickam V, Heydari Gharahcheshmeh M, Xu A, Zhang Y and Galstyan E 2015 *Supercond. Sci. Technol.* **28** 072002